A "Cold Path" for the Gulf Stream–Troposphere Connection

Benoît Vannière and Arnaud Czaja

Physics Department, Imperial College London, London, United Kingdom

Helen Dacre

Department of Meteorology, University of Reading, Reading, United Kingdom

Tim Woollings

Atmospheric Physics Clarendon Laboratory, Oxford University, Oxford, United Kingdom

ABSTRACT

The mechanism by which the Gulf Stream sea surface temperature (SST) front anchors a band of precipitation on its warm edge is still a matter of debate, and little is known about how synoptic activity contributes to the mean state. In the present study, the influence of the SST front on precipitation is investigated during the course of a single extratropical cyclone using a regional configuration of the Met Office Unified Model. The comparison of a control run with a simulation in which SST gradients were smoothed brought the following conclusions: a band of precipitation is reproduced for a single extratropical cyclone, and the response to the SST gradient is dominated by a change of convective precipitation in the cold sector of the storm. Several climatological features described by previous studies, such as surface wind convergence on the warm edge or a meridional circulation cell across the SST front, are also reproduced at synoptic time scales in the cold sector. Based on these results, a simple boundary layer model is proposed to explain the convective and dynamical response to the SST gradient in the cold sector. In this model, cold and dry air parcels acquire more buoyancy over a sharp SST gradient and become more convectively unstable. The convection sets a pressure anomaly over the entire depth of the boundary layer that drives wind convergence. This case study offers a new pathway by which the SST gradient can anchor a climatological band of precipitation.

1. Introduction

The long-term climatological impact of the SST gradient on the atmosphere has been identified both in observations and numerical experiments. The meanderings of the ocean fronts are tightly related to mesoscale features of the low-level atmosphere, such as the curl and divergence of wind stress (Xie 2004; Chelton et al. 2004) and cloud cover (Small et al. 2008). Minobe et al. (2008) proposed a climatological pathway by which the Gulf Stream SST gradient affects the troposphere above the boundary layer. The pressure in the marine atmospheric boundary layer (MABL) adjusts to the SST gradient and generates wind convergence that anchors a band of precipitation on the warm flank of the Gulf Stream. These results were obtained using reanalysis data and sensitivity experiments to SST at ½° resolution; when the SST gradient was smoothed the rainband disappeared. Minobe et al. (2010) highlighted the strong seasonality of precipitation and region of ascent; the maximum of anomalous precipitation that extends far offshore along the SST gradient during winter remains confined to the North American coast in summer. Moreover, while the mean vertical upward

---

Corresponding author e-mail: Benoît Vannière, b.vanniere@imperial.ac.uk

motion is deep during summer, it is rather shallow during winter, possibly a result of the more stratified troposphere in winter. Kuwano-Yoshida et al. (2010) also found that the precipitation response to the SST gradient was exclusively a result of convective precipitation.

The mechanism proposed by Minobe et al. (2008) is appealing since it combines all the mean climatological features of this region with simplicity. However, the relevance of such a mean state view can be questioned on the basis of Parfitt and Czaja (2016), who showed that synoptic systems have a direct contribution to time mean upward motion in the northwestern Atlantic. It has long been known that ocean fronts can influence synoptic storms, and we can surmise that they play a key role in the pathway connecting the SST gradient to the atmosphere. Sanders and Gyakum (1980) showed that explosive cyclogenesis occurs over a wide range of SSTs but, preferentially, near the strongest gradients. Giordani and Caniaux (2001) proposed the first detailed sensitivity analysis of how the Gulf Stream and its SST gradient affect, through surface turbulent fluxes and therefore the atmospheric boundary layer, frontogenesis and cyclogenesis. A strong sensitivity of an extratropical cyclone to prescribed SST anomalies was also demonstrated over the Kuroshio (Bond et al. 2010), but the results seem to be highly sensitive to other parameters such as large-scale circulation. In addition to the strength of storms, Field and Wood (2007) showed that the extratropical cyclone rain rate is strongly correlated with the underlying SST, in line with Clausius–Clapeyron argument. Moreover, the amount and the ratio of stratiform and convective precipitation, split according to a threshold rain rate of $5 \, \text{mm} \, \text{day}^{-1}$, strongly vary with SST (Giordani and Caniaux 2001).

The interaction of the upper ocean with the overlying atmosphere varies under different synoptic situations, such as cold and warm sectors of extratropical storms. On the one hand, the upward motion and the intense precipitation of warm conveyor belts make them obvious candidates to explain the favored ascent and the rainband of the Gulf Stream. On the other hand, heat fluxes are the strongest behind atmospheric cold fronts and south of the SST gradient, and they can be as large as $1000 \, \text{W} \, \text{m}^{-2}$ (Zolina and Gulev 2003) during intense cold air outbreaks (when cold and dry air coming from the continent is advected over the ocean). Moreover, the intensity of heat fluxes during winter cold air outbreaks was shown to be a function of the sharpness of the SST gradient (Sublette and Young 1996; Zolina and Gulev 2003). By contrast, in summer, heat flux variability was shown to be controlled by the absolute SST rather than the sharpness of the SST gradient (Zolina and Gulev 2003). Konda et al. (2010) showed that over the Kuroshio heat fluxes were also dependent on SST and atmospheric circulation.

Several recent studies have further investigated air–sea interactions in the frontal region under different synoptic situations. Young and Sikora (2003) revealed that the Gulf Stream meanders can generate mesoscale stratocumulus bands over its warm flank by initiating a tube-shaped circulation during cold outbreak. Liu et al. (2014) distinguished regimes of northerlies (reflecting cold air outbreaks) and southerlies; low-level cloud on the warm side of the Gulf Stream are more frequent under a regime of northerlies. Moreover, the composite of low-level cloud occurrence exhibited a circulation cell with ascending motion on the warm side of the front and descending motion on the cold side, which was thought to further contribute to the cross-frontal transition of low-level cloud-top height. Nelson and He (2012) found that over a period of 15 days with several cold air outbreaks, the Laplacian of sea level pressure (SLP) is well correlated with the wind divergence as was found for a 5-yr mean in Minobe et al. (2008). These three studies support a possible anchoring effect via the cold sector of extratropical storms. Yet, Minobe et al.'s (2008) mechanism has never been tested for an instantaneous event.

The mechanism leading to surface wind divergence or convergence with respect to SST fronts (Chelton et al. 2004) has been widely debated. Two distinct mechanisms have received large approval: namely, downward momentum mixing and boundary layer pressure adjustment. In the former mechanism, supported by de Szoeke and Bretherton (2004) and Skyllingstad et al. (2007), the enhanced turbulence on the warm side of the SST front brought eddy momentum downward, causing acceleration of low-level wind on the warm side of the Gulf Stream as observed by Sweet et al. (1981) and leading to wind convergence as in Wallace et al. (1989). In the latter mechanism, supported by Small et al. (2003), Cronin et al. (2003), and Minobe et al. (2008, 2010), the cross-gradient winds are pressure driven and due to the thermal adjustment of the boundary layer to the SST gradient, a mechanism similar to Lindzen and Nigam (1987) in the tropics. This mechanism was refined to account for the advection by the background atmospheric wind across the SST front, and it was found that the minimum of sea level pressure occurred downstream of the front (Small et al. 2005). Takatama et al. (2012, 2015) proposed an MABL model separating the role of the two mechanisms and concluded that pressure adjustment dominated over downward momentum mixing to explain the surface wind convergence. Some studies, however, reported that the sea level pressure signal could not be detected in observations (Hashizume et al. 2002; Tokinaga et al. 2005), whereas Cronin et al. (2003) and Plagge et al. (2016) argued that despite being weak, this

signal could play a significant role over small length scales. In an attempt to reconcile the two views, it was suggested that both mechanisms may play a role under different background regimes (Spall 2007; Small et al. 2008): if the background wind is weak, the boundary layer has time to adjust thermally to SST and wind acceleration on the warm side can be pressure driven; this is, however, not the case under stronger advection. In addition, the resolution of models and their vertical extent used to investigate these processes (Small et al. 2008; Skyllingstad and Edson 2009) modify the general balance in the momentum equation, with low and high resolution favoring, respectively, pressure adjustment and downward momentum mixing.

In addition to surface wind convergence or divergence, some numerical studies reported a secondary cell with convergence and ascent on the warm side of the SST front (Huang and Raman 1988; Wai and Stage 1989; Brachet et al. 2012). This circulation may well participate together with vertical turbulent fluxes to increase the depth of the boundary layer. However, Song et al. (2006) showed that opposite results were obtained in observations: the acceleration of wind over the SST gradient under cold to warm airflow caused divergence. The subsidence associated with surface divergence was thought to entrain air from the free troposphere in the boundary layer.

Few studies investigated in detail the link between the front and the enhanced precipitation on the warm side of the Gulf Stream. One could expect the mean ascent in the frontal region to be associated with condensation of moisture and precipitation as suggested by Minobe et al. (2008). But a direct response to SST forcing independent of the secondary circulations generated near the front might also be possible. Such a response was investigated by Skyllingstad and Edson (2009) using a quasi-Lagrangian framework: two experiments were carried out in which spatially uniform SSTs were respectively maintained constant and increased in time so as to simulate the effect of air passing over the SST front. In the two experiments, the growth of the boundary layer was forced by radiative cooling, large-scale rain reevaporation, and mechanical entrainment. When SST was uniformly varied in the domain, there was more convective precipitation and turbulence than in the experiment with constant SST. These results are in agreement with observations; Wayland and Raman (1989) reported a change of turbulence across the SST gradient, and organized convection has been noticed.

The strong variability of air–sea interactions with synoptic regimes and the lack of a clear pathway linking the Gulf Stream SST front to its anchored rainband provide two motivations to 1) test whether Minobe et al.'s (2008) mechanism remains true for instantaneous events and 2) assess the mechanisms providing the precipitation enhancement along the front at synoptic time scale.

The goal of this paper is to show that the influence of the Gulf Stream SST gradient on precipitation can be reproduced for a single synoptic event, where it occurs mainly in the cold sector of storms, and we will propose a mechanism explaining this. The remainder of the paper is organized as follows: in section 2 we present data and methods, in section 3 the event chosen for the case study is described, in section 4 we show that sensitivity experiments similar to Minobe et al. (2008) can be reproduced with a single synoptic event, in section 5 we suggest a mechanism to show how the cold sector interacts with the SST gradient, and finally we summarize and discuss the findings in section 6.

2. Data and method

a. Model and case study

The Met Office Unified Model (UM), version 7.3, is a finite-difference model that solves the nonhydrostatic, deep-atmosphere dynamical equations with a semi-implicit, semi-Lagrangian integration scheme (Davies et al. 2005). The model uses Arakawa C staggering in the horizontal (Arakawa and Lamb 1977) and is terrain following in the vertical with a hybrid-height coordinate and Charney–Phillips staggering (Charney and Phillips 1953). A rotated horizontal grid is used in the limited-area model (LAM) configuration, which has one-way nesting from the global model. The parameterization of physical processes includes longwave and shortwave radiation (Edwards and Slingo 1996). A nonlocal mixing scheme is used for unstable boundary layers (Lock et al. 2000). Convection is parameterized: the convection scheme used is a mass flux scheme based on Gregory and Rowntree (1990) with extensions to include downdrafts (Gregory and Allen 1991) and convective momentum transport (CMT; Gregory et al. 1997; Stratton et al. 2009). The scheme diagnoses three regimes of convection: deep and shallow convection, starting from the boundary layer, and midlevel convection operating above. The deep convection is triggered by the instability of lifting a surface parcel. The deep and midlevel convection use a closure based on CAPE, with a vertical-velocity-dependent CAPE time scale. The reference time scale for CAPE removal is set to 30 min and the threshold of vertical velocity for CAPE dependence to $1 \, \text{m s}^{-1}$. The microphysics is a mixed-phase scheme including prognostic ice and liquid water (Wilson and Ballard 1999).

For the case study, we chose an extratropical cyclone which traveled eastward over the western North Atlantic Ocean basin from 15 to 17 January 2004. The synoptic conditions of the case study are further described in section 3. The Met Office UM has been run in a global configuration at a resolution of 40 km to generate the boundary conditions of the nested North Atlantic (NA) domain (resolution 12 km). Two simulations, CNTL and SMTH, are forced by two different sets of SST. CNTL and SMTH share the same lateral boundary conditions and differ only by the prescribed SST. SST is taken from ECMWF operational analysis at 0.25° and interpolated linearly to the model's resolution (12 km). CNTL is forced by the instantaneous SST of 14 January 2004, which is kept constant for the rest of the simulation. SMTH SST forcing was produced by smoothing out CNTL SST using a simple spatial filter, in which each point is a weighted average of itself and its four immediate neighbors. The filter was applied in a box centered on the Gulf Stream SST front with a Gaussian transition to the region outside the box where no smoothing is applied. This spatial filter was applied 3000 times at each grid point. The same technique was used in Minobe et al. (2008) to generate smoothed SST. Typical values of the SST gradient in the frontal region are 5 and 2 K $(100\,\mathrm{km})^{-1}$ in CNTL and SMTH, respectively. The model was initialized on 14 January 2004 at 1200 UTC and integrated over 72 h. The initial conditions were provided by the ECMWF operational analysis (ECMWF 2011).

The use of a nonhydrostatic model is required to model the mesoscale convective systems occurring in the cold sector during a cold air outbreak. The finer resolution of the model outputs presented in this study is 12 km. We conducted CNTL and SMTH experiments at 4 km in a smaller domain centered over the SST front. At this resolution, precipitation is entirely resolved by the model. The difference of precipitation between CNTL and SMTH is similar to the difference simulated at 12 km. Similarly, we found a circulation cell across the SST front at 4 km similar to the one simulated at 12 km.

b. Cold-sector indicator

To partition a given variable inside and outside the cold sector, we use the indicator combining PV and sensible heat flux presented in Vannière et al. (2015) to limit the spurious detection of the warm conveyor. This double criterion was shown to be the most accurate to rightly attribute precipitation and subsidence to the cold sector in a composite of 57 storms. More specifically, it was shown to limit the wrong attribution of large-scale precipitation occurring in the warm conveyor belt to the
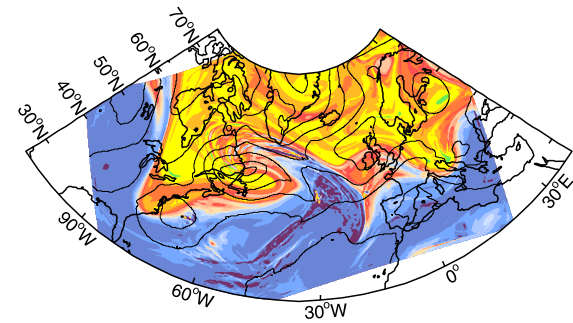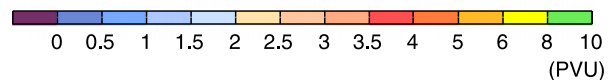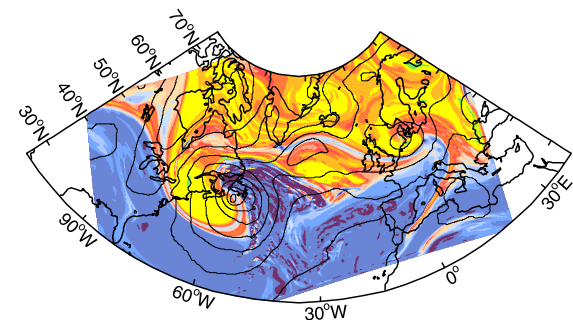

FIG. 1. Synoptic view of the storm at 1200 UTC on (a) 15 and (b) 16 Jan 2004 simulated by the UM in the NA domain. PV (in PVU; $1\,\mathrm{PVU} = 10^{-6}\,\mathrm{K\,kg^{-1}\,m^2\,s^{-1}}$) on the isentropic surface 315 K (color shading). Sea level pressure (black contours; contour interval of 5 hPa). (Note that PV at surface is used to compute the cold-sector mask and should not be compared to this figure.)

cold sector. The cold-sector mask is set to unity when PV at 975 mb (1 mb = 1 hPa) is negative and sensible heat flux is larger than a given threshold and set to zero otherwise. A sensible heat flux threshold of $50\,\mathrm{W\,m^{-2}}$ is used as in Vannière et al. (2015) for ERA-Interim data. We refer the reader to this latter study for a thorough discussion of the accuracy and robustness of the masking method.

3. Overview of the cold air outbreak event in the case study

a. Synoptic conditions of the case study

Figure 1 gives a synoptic view of the extratropical cyclone selected for the case study. After 24 h of simulation, on 15 January 2004 at 1200 UTC, a fold of the tropopause associated with a planetary wave is passing over the east coast of North America. It coincides with a low-level cyclone at 50°N, 60°W, identified by a
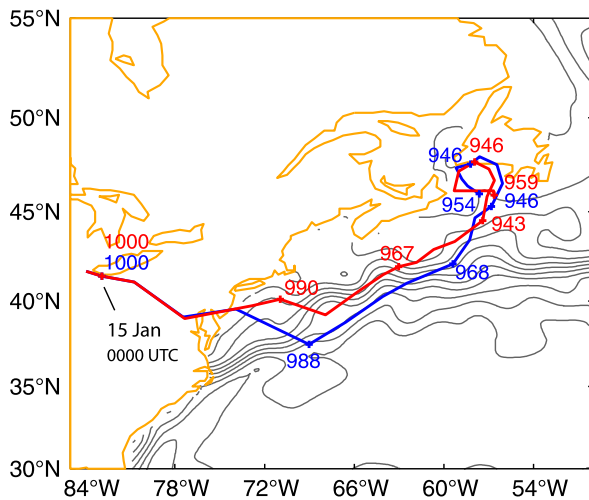
FIG. 2. Track of the extratropical cyclone lowest pressure in CNTL (blue) and SMTH (red) from 15 Jan 2004 at 0000 UTC. Lowest pressure is given in hectopascals and in the respective color of each simulation from 15 Jan 2004 at 0000 UTC and every 12 h after. The gray contours represent CNTL SST (every 2 K).

minimum of sea level pressure. One day later, on 16 January, the upper- and low-level cyclones have mutually amplified and moved eastward; the minimum of SLP is now located over Nova Scotia. At that time and during the next 24 h, the entire Gulf Stream SST front is located in the cold sector of the storm. The propagation and magnitude of the lowest pressure in CNTL and SMTH are similar in the two simulations.

The track of the cyclone and its deepening rate are, however, slightly altered by the prescribed SST (Fig. 2). On 15 January, the lowest pressure is on the northeastern North American coast. In the next 24 h, the extratropical cyclone experiences an explosive development characteristic of the so-called "bomb storm" with a deepening rate of $32\,\mathrm{hPa\,day}^{-1}$ [note that the deepening rates are not scaled by $\sin\phi$, where ϕ is the latitude, as sometimes done (e.g., Sanders and Gyakum 1980)]. During the first 12 h of 15 January, the lowest pressure moves southeastward on the warm side of the SST front, before traveling northeastward toward Newfoundland on the second half of that day. On 16 January, the storm continues deepening at a rate of $27\,\mathrm{hPa\,day}^{-1}$. In SMTH, the track of the cyclone is shifted by 1°–2° of latitude north of its track in CNTL. Note that in SMTH the SST is warmer than in CNTL north of the SST front. Even though the cyclone deepening rate is larger in CNTL than in SMTH during the first half of 15 January, the opposite is observed during the second half of that day.

b. Precipitation

The total precipitation simulated by CNTL over the three days of the experiment (Fig. 3a) is the largest south of the

SST gradient and reaches $25\,\mathrm{mm\,day}^{-1}$. Total precipitation in CNTL is compared to TRMM real-time observations (Fig. 3b). The pattern of precipitation, with a maximum south of the SST front, reaching the same amplitude as in CNTL, is well captured. A few discrepancies can be noticed. As TRMM cannot detect light rain (Huffman et al. 2007), it does not feature the low precipitation rates simulated by CNTL directly off the North American coast. Moreover, TRMM shows a higher precipitation rate in the northeastern part of the domain. The overall good agreement between CNTL and TRMM precipitation allows us to investigate the physical processes in more detail.

Total precipitation is further split into precipitation occurring outside and inside the cold sector (Figs. 3c and 3d, respectively), which corresponds mainly to the warm conveyor belt (WCB) precipitation. The precipitation in the two regions is partitioned using the cold-sector indicator described in section 2b. Precipitation occurring outside the cold sector covers a large area and corresponds to the WCB transiting through the domain. However, a substantial amount of precipitation occurs in the cold sector, reaching a maximum of $10\,\mathrm{mm\,day}^{-1}$ for the average of the three days of the case study. Moreover, precipitation occurring in the cold sector is located in a band of 5° of latitude south of the SST front, contrary to WCB precipitation that shows only little connection with the SST front.

We show the contribution of the large-scale and convective rain in Figs. 3e and 3f, respectively (note that each has a contribution from the warm and cold sectors). Even though this decomposition is sensitive to the resolution of the model, the large-scale precipitation scheme, and the convective parameterization, it can help infer the physical processes leading to precipitation. We draw the reader's attention to the fact that precipitation in Fig. 3a, which is found in neither Fig. 3e nor Fig. 3f, corresponds to snow. Convective rain is situated mainly south of the SST front and peaks close to the front, whereas large-scale rain is mostly along and north of it. Interestingly, the detail of this distribution is consistent with the long time average described in Kuwano-Yoshida et al. (2010). The comparison of Fig. 3c to Fig. 3f shows that south of the gradient, the WCB precipitation is mainly made of convective rain, whereas over the SST gradient, it is made of large-scale rain. This split corresponds, respectively, to the low-level and ascending branches of the WCB. It is not surprising that as isentropic surfaces are steeper over the SST front, ascent is favored and drives large-scale precipitation. The precipitation in the cold sector is mostly made of convective rain.

The close connection of convective rain in the cold sector with the SST front together with the numerous studies mentioned in the introduction, suggesting key
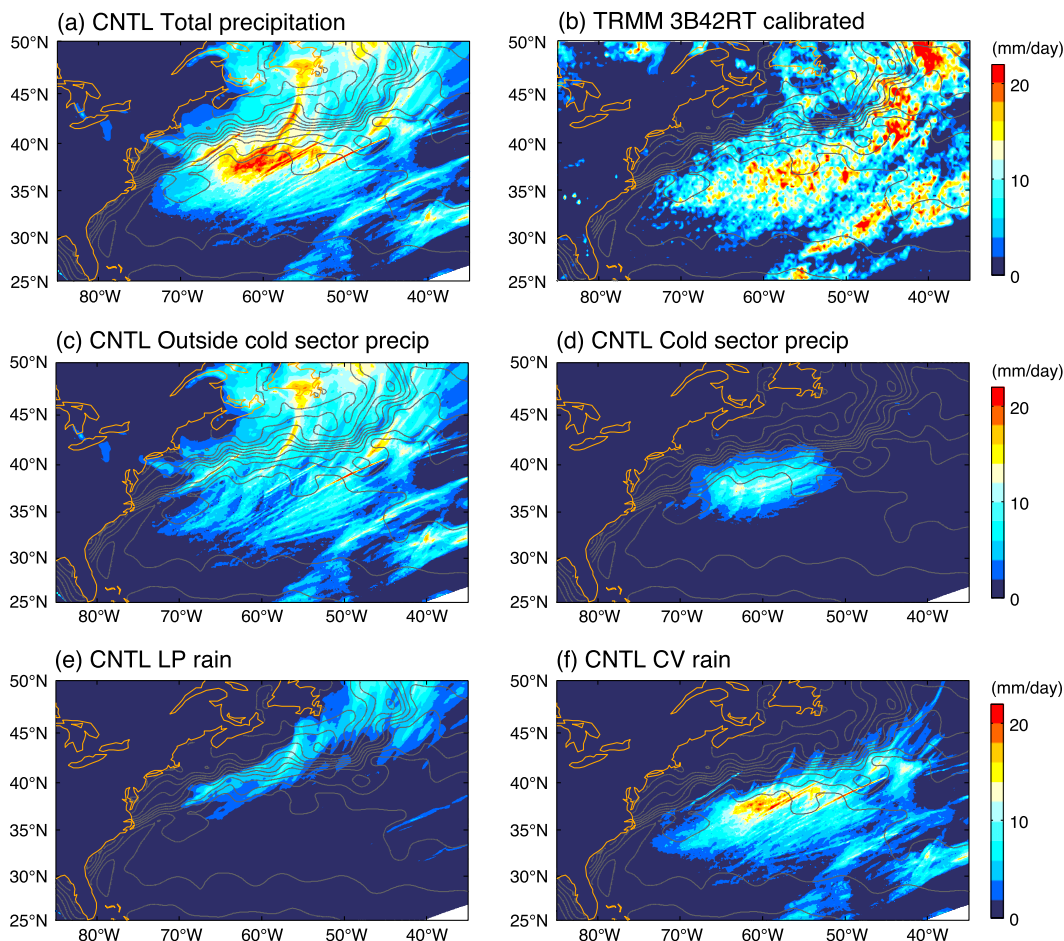
FIG. 3. (a) Total precipitation in CNTL. (b) TRMM real-time and calibrated precipitation. CNTL precipitation is decomposed in (c) precipitation occurring outside the cold sector, (d) precipitation occurring in the cold sector, (e) large-scale rain, and (f) convective rain. All precipitation (mm day^{-1}) is averaged over the three days of the case study . See text for detail of the partitioning between inside and outside the cold sector. The gray contours represent CNTL SST (every 2 K).

interactions between the atmosphere and the SST front in the cold sector, provides motivation to focus more deeply on the cold sector in the rest of the paper. In the next section, we investigate more specifically circulation changes associated with the convective rain in the cold sector.

c. Circulation

We found that CNTL exhibits a region of ascent in the lower troposphere in the cold sector east of 65°W (Fig. 4, bottom), which is collocated with the convective precipitation (cf. with Fig. 3d). At 700 mb and west of 65°W, the air is subsiding as is generally the case in the cold sector. A longitudinal section through the region of ascent is shown in Fig. 4, top. The cold-sector subsidence west of 65°W and the strong ascent of the WCB at

approximately 40°W extend vertically throughout the troposphere. Between them, the cold-sector ascent reaches the midtroposphere only.

4. Interaction of an extratropical cyclone with the Gulf Stream SST front

a. Precipitation response

In this section, we follow the modeling strategy of Minobe et al. (2008) and investigate the sensitivity of air–sea interactions in the extratropical cyclone described in section 3 to a smoothing of the SST gradient.

In Fig. 5a, we present the total precipitation in SMTH. The overall pattern resembles the one in CNTL (Fig. 3a). The regions away from the smoothed SST
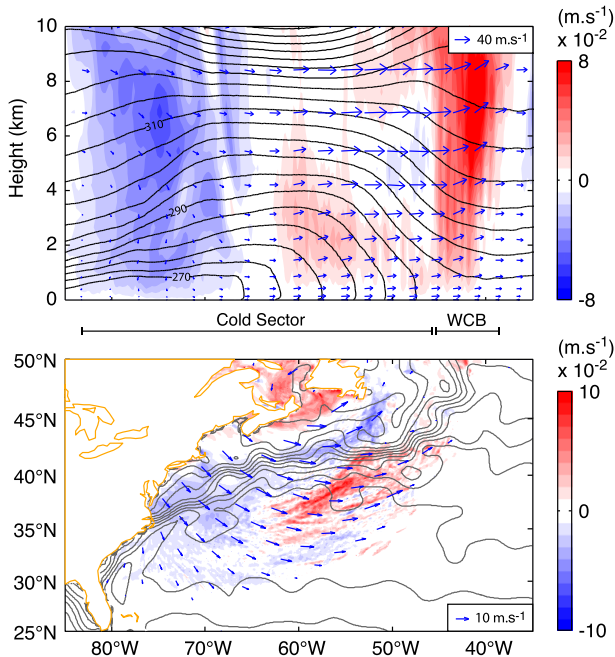
FIG. 4. (top) Zonal cross section of wind in CNTL (arrows) and vertical wind only (colors) averaged between 36° and 42°N. Potential temperature (every 4 K) is overlaid in black lines. (bottom) Vertical wind at 700 hPa in the cold sector in CNTL. The cold-sector contribution was selected by applying the cold-sector mask and WCB's contribution is not shown. Arrows stand for 10-m wind vectors. The gray contours represent CNTL SST (every 2 K). All the diagnostics are 24-h averaged over the third day of the simulation.

gradients are very similar, but the sharp maximum that was simulated on the south edge of the SST front has disappeared. As in CNTL, there is precipitation in the cold sector in SMTH (Fig. 5b), but the magnitude is weaker and it extends farther northward (cf. with Fig. 3d). The difference in total precipitation between CNTL and SMTH is partitioned between the cold sector and outside the cold sector in Figs. 5c,d. The difference in precipitation outside the cold sector is relatively noisy, as can be expected over such a short period of time. It is made of alternating positive and negative anomalies, which correspond to the slight displacement of the frontal region between the two simulations. There is no clear relation between this difference and the SST front, except around 70°W where a northward shift of precipitation is observed in SMTH. In contrast to this, the difference in precipitation in the cold sector forms a coherent dipole of anomalous precipitation, with enhanced precipitation over the warm side of the SST gradient in CNTL and reduced precipitation over the cold side. The precipitation anomaly reaches 10 mm day^{-1} in CNTL (Fig. 5c) and is mostly formed of convective rain (not shown).

These results have many implications. First, they show that a modulation of precipitation by the SST front is already noticeable in a single synoptic event. Hence, a case study may shed relevant insight into mechanisms. Second, the effect of the SST gradient is mostly found on convective precipitation, which is also the case in a long and stabilized simulation, as shown by Kuwano-Yoshida et al. (2010), giving credence that similar processes are at work. Finally, given that convective precipitation is also simulated in SMTH in the cold sector, the main effect of the SST gradient is to modulate the amount of convective precipitation rather than initiating the development of cumulus convection. Note that the change in precipitation between CNTL and SMTH might be underestimated in our study as the SST gradient has not been entirely removed in the SMTH experiment.

In an attempt to identify the mechanism setting the anomalous precipitation, we analyzed the vertically integrated moisture budget in the region where convective precipitation in CNTL is enhanced. The detail of the analysis is not shown but we here summarized the main conclusions. We found that surface wind convergence has a primary role in supplying moisture for the anomalous convective precipitation. This relation supports that of Minobe et al. (2008) between surface wind convergence and excess of precipitation on the south side of the SST front. In section 5, we will show that the difference in surface fluxes between CNTL and SMTH modulates the convection on both sides of the SST gradient and creates the dipole of anomalous convective precipitation.

b. Dynamical response to the SST gradient

As briefly reviewed in section 1, several studies showed that pressure adjustment in the boundary layer is the principal mechanism leading to surface wind convergence and ascent on the warm side of the Gulf Stream. This relationship was demonstrated for a 5-yr mean by Minobe et al. (2008) but also for a shorter period of time such as a few weeks of cold air outbreak by Nelson and He (2012). In this section, we investigate if the pressure adjustment mechanism still holds over one day of cold air outbreak.

The anomalies of vertical wind at 700 mb and surface wind divergence due to the SST front are presented in Fig. 6. As the spatial derivatives are very sensitive to noise, a Lanczos filter in two dimensions (Lanczos 1988) was applied to data, after taking the difference between CNTL and SMTH and before applying the spatial derivative in the case of divergence. The cutoff wavelength is 6×10^{-3} km, and the width of the transition band is 4×10^{-3} km. The difference of vertical wind at 700 mb between the two experiments (Fig. 6a) forms a dipole slightly downstream of the precipitation dipole (Fig. 5c).
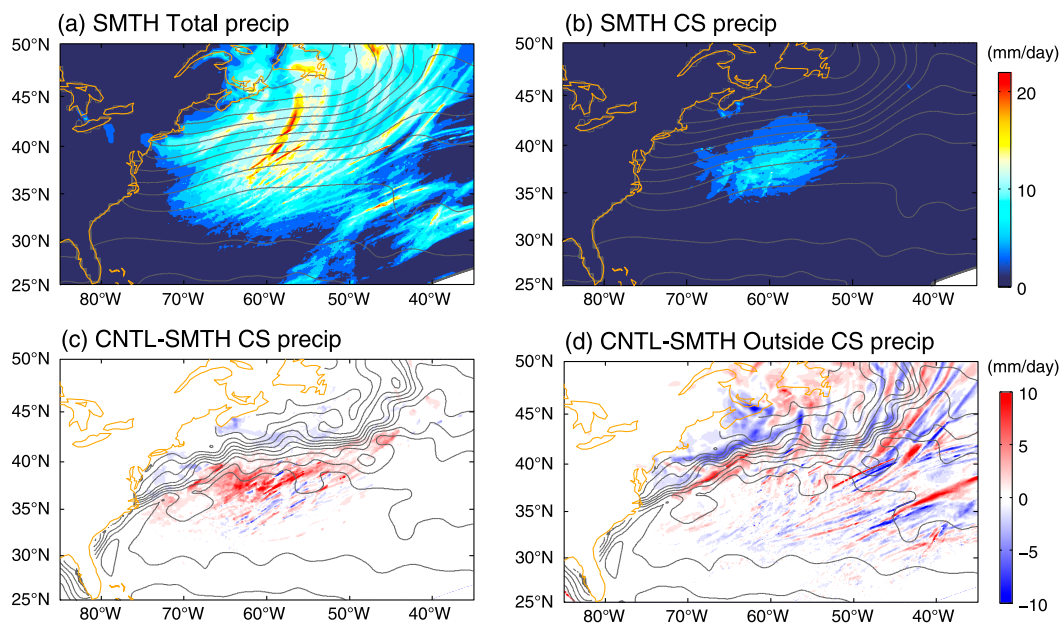
FIG. 5. (a),(b) As in Fig. 3a,d, but for SMTH. Difference between CNTL and SMTH in (c) cold sector and (d) outside the cold-sector precipitation (see text for further explanation). All precipitation (mm day^{-1}) is averaged over the three days of the case study.

Surface wind divergence forms a dipole identical to that of vertical ascent (Fig. 6b).

As for the long-term mean (Minobe et al. 2008), there is an overall good collocation of the dipole of Laplacian of SLP (Fig. 7a) and surface wind convergence at the time scale of one synoptic event. However, slight differences are observed; the Laplacian of SLP follows the SST gradient from the North American coast, whereas surface wind convergence is significant only west of 65°W. This suggests that in the particular conditions of a cold air outbreak, the balance suggested by Minobe et al. (2008) might be more complicated. In the following sections, we will propose that it is the pressure anomalies set by convection that drive the surface wind convergence on the warm side of the SST front during cold air outbreaks.

Several studies proposed boundary layer models using the approximation that the Laplacian of SLP is proportional to the Laplacian of SST (Minobe et al. 2008). This is based on many assumptions and in particular that there is no lag in the response of the boundary layer to the SST. However, other studies found only very small correlations between the instantaneous fields of the Laplacian of SST and surface wind convergence (J. Small 2016, personal communication). This is also the case here where the nonfiltered Laplacian of SST is poorly correlated with the Laplacian of SLP (not shown). We found, however, a better correlation for the spatially filtered Laplacian of SST (Fig. 7b). This suggests that structures on a spatial scale larger than the

typical size of an oceanic eddy might be more relevant to this problem.

Figure 8 shows the difference of wind between CNTL and SMTH in a meridional section zonally averaged between 65° and 45°W. An anomalous circulation cell is oriented north–south, perpendicular to the cold air outbreak mean flow and centered over the maximum SST anomaly (cf. Fig. 4, bottom). The cell is centered on the SST gradient, with anomalous surface wind flowing southward and wind above the top of the boundary layer flowing northward. The cell is reminiscent of the mean anomalous circulation found by Brachet et al. (2012) when the SST gradient is strengthened. Enhanced ascent in CNTL up to 500 mb is consistent with both Minobe et al. (2010) and Brachet et al. (2012).

In conclusion, the anomalous convergence of surface wind, the ascent on the warm edge of the SST front, and the circulation cell perpendicular to the SST gradient, which were described as mean state features of the Gulf Stream frontal region in several previous studies (see the introduction), also occur in the cold sector of a single storm. The role of the cold sector in setting the anomalous precipitation (section 4a) and the anomalous circulation (this section) response to the SST front provides motivation to revisit the pressure adjustment mechanism to account for the role of the strong surface turbulent fluxes and convection occurring in this part of the extratropical cyclone. This is done in the following section.
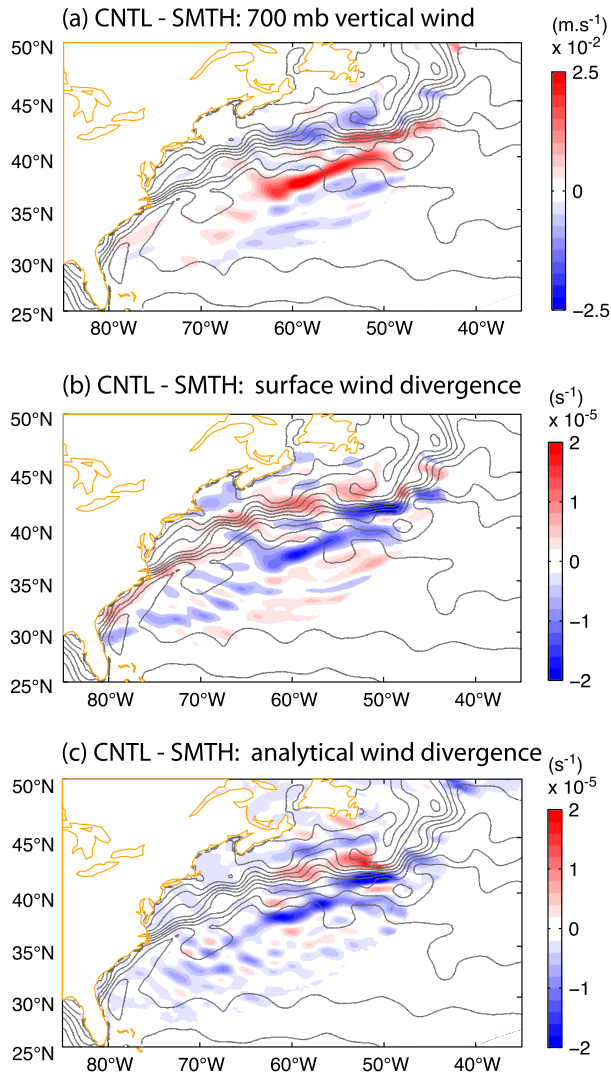
FIG. 6. (a) Difference in vertical wind at 700 mb and (b) surface wind divergence between CNTL and SMTH in the cold sector and averaged over the third day of case study. (c) Difference in surface wind divergence between CNTL and SMTH estimated from the analytic formula in Eq. (3). Data in (a)–(c) are filtered using the Lanczos spatial filter. The gray contours represent CNTL SST (every 2 K).

5. A boundary layer model linking the SST differences to precipitation and circulation change

In this section, we build a diagnostic MABL model to explain in simple steps the mechanism responsible for the enhanced convection in the cold sector. We first evaluate the combined effect of sensible and latent heat fluxes on the integrated moist entropy as cold-sector air parcels flow over the ocean (section 5a). Then, the difference of moist entropy is related to the change of convective available potential energy (CAPE) (section
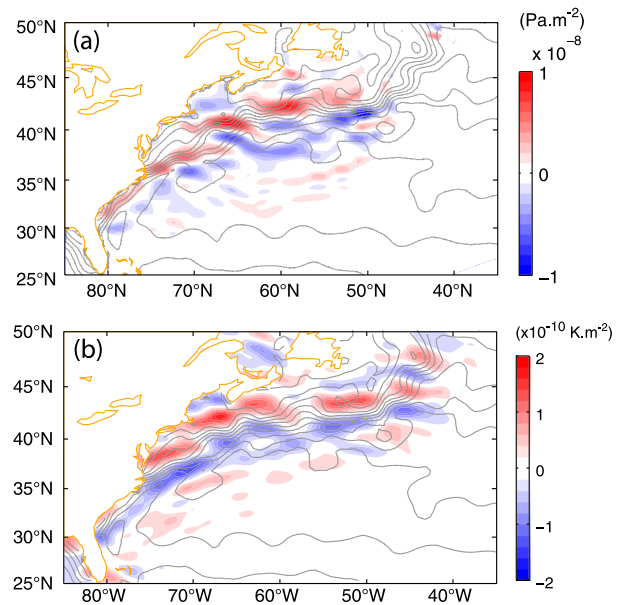

FIG. 7. (a) Difference in Laplacian of pressure difference between CNTL and SMTH averaged over the third day of case study using sea level pressure (Pa m^{-2}). The gray contours represent CNTL SST (every 2 K). (b) As in (a), but for the difference in Laplacian of SST (K m^{-2}). Data in (a),(b) are filtered using the Lanczos spatial filter.

5b). Finally, we show that the boundary layer pressure anomaly set by convective adjustment drives the circulation cell in the cold sector (section 5c). The diagnostic model is tested against the results of the UM to verify that it captures the essential convective and dynamical responses to the SST gradient.

a. Entropy changes in the boundary layer

In the diagnostic MABL model presented here, the surface moist entropy plays a central role. Moist entropy is modified by heat and moisture uptake as parcels move over the sea surface, and when saturated, it can be related in a simple manner to local CAPE (Emanuel 1994).

Figure 9 shows the turbulent heat fluxes in CNTL (contours) and their difference with SMTH (shadings) in the cold sector of the extratropical storm only. Sensible and latent heat fluxes reach, respectively, 500 and 800 W m^{-2} in CNTL, and their maxima are located near the coast where the air–sea temperature and humidity contrasts are largest. As expected, the effect of the SST gradient is to enhance surface turbulent fluxes on the warm side of the front in the western part of the ocean basin. Interestingly, though, there are two negative anomalies of surface turbulent heat fluxes in CNTL south and north of the positive anomaly. This tripole
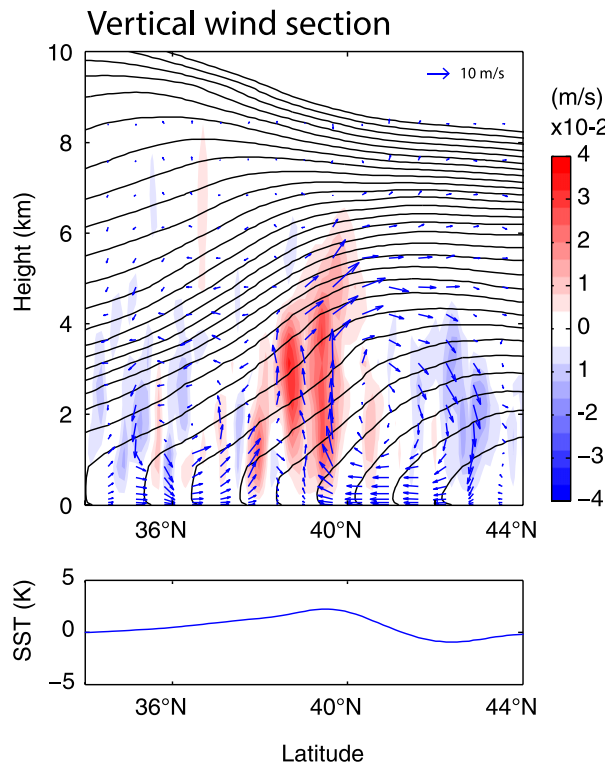
Vertical wind section

FIG. 8. (top) Meridional cross section of the difference between CNTL and SMTH in wind (arrows) and vertical wind (color shading) averaged between longitudes 65° and 45°W over the third day of the simulation. Potential temperature (every 2 K) is overlaid in black contours. (bottom) CNTL minus SMTH SST (K) averaged over the same range of longitudes as fields in (top).

FIG. 9. Surface turbulent in (a) sensible and (b) latent heat fluxes (W m^{-2}) in CNTL (black contours) and their difference with SMTH (color shading) over the third day of the case study. The gray contours represent CNTL SST (every 2 K).

pattern is due to the fact that turbulent fluxes are not only a function of SST but also of the time-varying boundary layer physical properties. In CNTL, the sudden increase of SST leads to an increase of turbulent heat fluxes just downstream of the SST front. However, farther downstream, the SST seen by the parcel levels off and the turbulent fluxes are weaker in comparison to SMTH. Moreover, we note that the difference in convective precipitation is located farther downstream of the maximum heat flux anomaly (see Fig. 5), suggesting that the air mass needs to accumulate moisture and heat before becoming unstable. The tripole pattern of anomalous heat fluxes and especially the reduction of turbulent heat fluxes south of 35°N may amplify the banded pattern of anomalous convective precipitation.

To relate the change of moist entropy to the turbulent heat fluxes, we compute 2D (i.e., horizontal motion in the boundary layer) backward trajectories of parcels from the cold sector. Trajectories are found by solving the kinematic equation. We use a first-order finite difference to discretize the time derivative. The trajectory of each parcel is integrated backward in time from its final
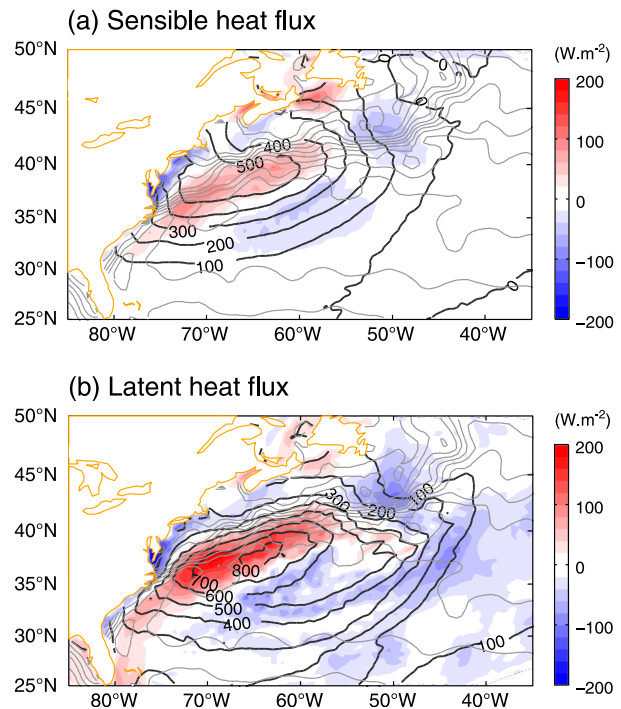
position, which is chosen to be every 0.5° in longitude and latitude over the domain 35°–50°N, 70°–40°W. The advection term is calculated using the mean wind in the boundary layer from CNTL. The tendencies of temperature and humidity in the boundary layer are obtained by assuming that air is homogeneously warmed and humidified by surface turbulent fluxes up to the MABL top. The temperature and humidity of air parcels are then found by summing those instantaneous tendencies, forward in time, along the trajectories previously computed. The temperature and humidity are then used to calculate the moist entropy of air parcels (Emanuel 1994). In Fig. 10a, we present the difference in moist entropy between CNTL and SMTH for the 2000 parcels at the end of their trajectories. As expected moist entropy is enhanced on the warm side of the Gulf Stream by almost 20 J K^{-1} kg^{-1}. Heat flux integration along parcel trajectories captures the difference of moist entropy calculated as a function of state directly from model outputs at the end of the third day (Fig. 10b). The difference of moist entropy is slightly overestimated by parcel integration as entrainment of dry air at the top of the boundary layer and subsidence were disregarded in the integration. This analysis shows that the history of turbulent heat fluxes seen by parcels is the primary factor explaining the
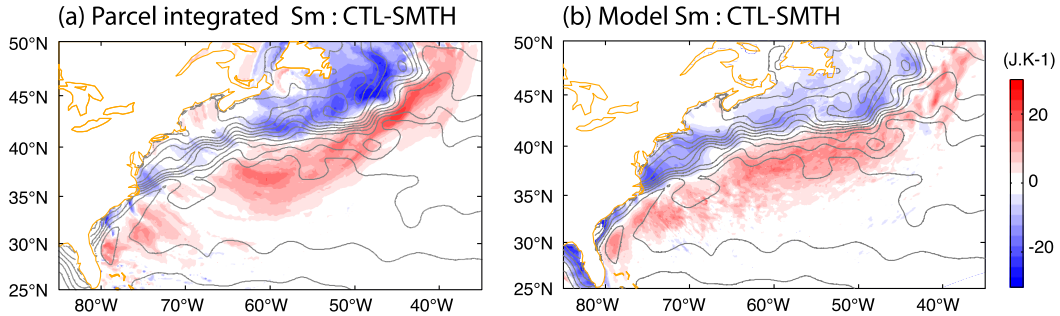
FIG. 10. Difference in boundary layer moist entropy ($J\,K^{-1}$) in CNTL and SMTH at the end of the third day of the case study: (a) Boundary layer entropy obtained by the integration forward in time of turbulent heat fluxes along Lagrangian trajectories. (b) Boundary layer entropy calculated as a function of state with model outputs. The gray contours represent CNTL SST (every 2 K).

difference in moist entropy simulated between the two experiments.

b. Modulation of convection

We now try to relate the difference in entropy in the boundary layer to the local difference in CAPE. Emanuel (1994) showed that CAPE can be expressed in terms of entropy using Maxwell's relation:

$$\text{CAPE} = \int_{T_{\text{LFC}}}^{T_{\text{LNB}}} (s_p - s_{\text{env}})\, dT, \quad (1)$$

where T_{LFC} is the temperature at the level of free convection (LFC), T_{LNB} is the temperature at the level of neutral buoyancy (LNB), s_p is the entropy of the ascending parcel, and s_{env} is the entropy of the environment. The advantage of using entropy in the formulation of CAPE is that s_p is conserved during the moist adiabatic ascent and is thus equal to the surface saturated moist entropy s_{0*}. We make the assumption that the difference in temperature at the level of free convection between CNTL and SMTH is close to the difference in temperature at the level of neutral buoyancy. In other words, we assume that the temperature profile is shifted by the same amount over the

vertical and that the depth of the convection is not significantly affected. We can then compute the difference in CAPE between the two simulations as follows:

$$\text{CAPE}' \approx -s'_{0*}(T_{\text{LFC}} - T_{\text{LNB}}) - \int_{T_{\text{LFC}}}^{T_{\text{LNB}}} s'_{\text{env}}\, dT, \quad (2)$$

where the primes denote the difference between CNTL and SMTH. The first term on the rhs gives its sign to CAPE′, whereas the second, accounting for the difference in the environment in the two simulations due to the convective adjustment upstream, will partly compensate the first term. This equation is interesting as it emphasizes the link between the anomalous low-level entropy, a physical property that can be related back to the history of parcels passing over SST (see section 5a), and the difference in CAPE between CNTL and SMTH.

The difference in CAPE between CNTL and SMTH output directly from the model (Fig. 11a) is now compared with the difference in CAPE calculated analytically with Eq. (2) (Fig. 11b). UM CAPE is larger by up to $50\,J\,K^{-1}$ on the warm edge of the front in CNTL and reduced by the same amount north of the front (Fig. 11a). The difference in analytic CAPE captures
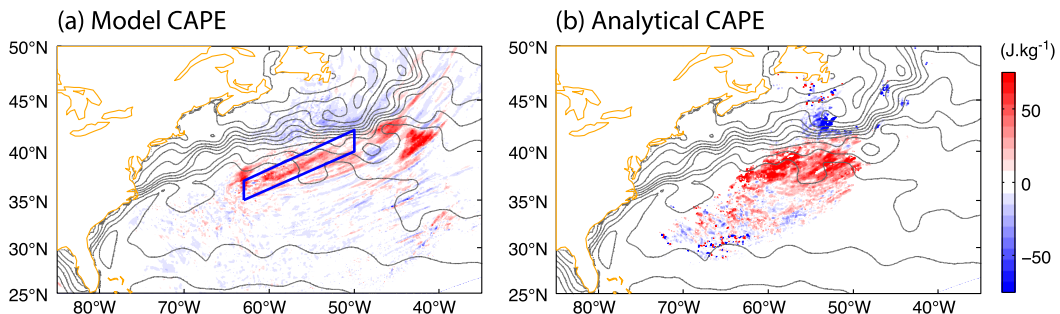

FIG. 11. Difference of CAPE in CNTL and SMTH over the third day of the case study with (a) CAPE from UM and (b) CAPE recalculated with the analytic formula in Eq. (2). The gray contours represent CNTL SST (every 2 K). [The box in (a) is used to compute the CAPE and precipitation averaged in Fig. 12.]
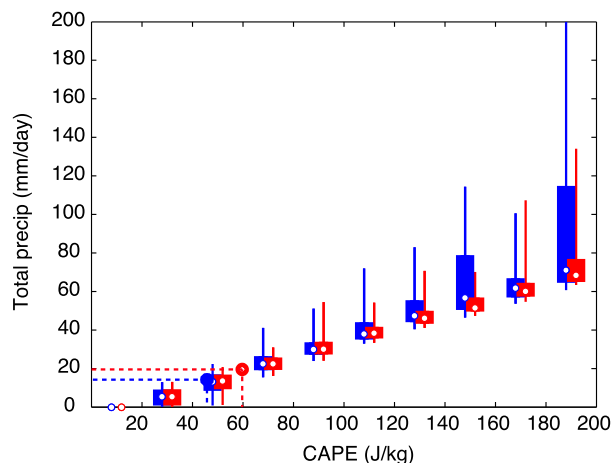
FIG. 12. Mean distribution of convective precipitation amount as a function of CAPE for each grid point of CNTL (blue) and SMTH (red) simulation. The box and whiskers depict the following information: the median (white dot), the 1st and 3rd quartile (upper and lower box limits), and the 1st and 9th decile (upper and lower bar limits). The blue and red dots for CNTL and SMTH, respectively, are obtained by averaging the quantities in the box depicted in Fig. 11.

to a large extent the difference in CAPE calculated by the UM; the amplitude of the dipole is of the same order of magnitude, and the largest value of the difference is found around 60°W. As could be expected, the analytic CAPE is overestimated compared to UM CAPE, implying that there is no downdraft or air entrainment taken into account that could inhibit convection.

We want to test if the change of CAPE on the warm flank of the Gulf Stream can explain the increase in convective precipitation. To do so, we have computed the distribution of convective precipitation as a function of UM CAPE (Fig. 12). We used hourly averaged CAPE and convective precipitation by sampling all the model time steps (every 12 min) over the third day. To test whether our diagnostics are scale dependent, the binning was tested for single grid points (12-km resolution), by averaging a square of nine contiguous grid points (36-km resolution) and by averaging a square of 25 contiguous grid points (60-km resolution). Each of the three diagnostics gives the same linear relation between precipitation and CAPE. So there is no scale dependence of our diagnostic. (Note that the variance of precipitation tends to increase for bins of large CAPE; however, the number of points that fall in those bins being relatively small, it is difficult to conclude why it is so.) Moreover, the same linear relation is observed in both CNTL and SMTH. Figure 12 shows CAPE and precipitation in the box depicted in Fig. 11 for both CNTL (blue dot) and SMTH (red dot). The two points lie on the linear fit; therefore, the anomalous precipitation can be directly related to the anomalous CAPE in the box: an

increase of CAPE of $15\,\mathrm{J\,K^{-1}\,kg^{-1}}$ as observed on the warm side of the SST gradient corresponds approximately to an increase of precipitation of $7\,\mathrm{mm\,day^{-1}}$, which is consistent with Fig. 5c.

The results of this section confirm that the SST gradient modulates the entropy of the parcels flowing in the cold sector and enhances CAPE on the warm side of the SST gradient, thus leading to the formation of an anomalous band of precipitation.

c. Dynamical response

The impact of the SST front on low-level convergence remains to be understood. Here, we assess if the pressure anomaly set by convection can drive the surface wind convergence and anomalous circulation cell discussed in section 4. To that end, we have revisited the MABL model proposed by Minobe et al. (2008; the detail of the calculation is given in the appendix) to account for the role of convective adjustment in the boundary layer. The following equation relates the difference in surface wind divergence $\nabla \cdot \mathbf{v}_0'$ in the boundary layer to the difference in surface saturated moist entropy s_{0*}':

$$\frac{\varepsilon^2 + f_0^2}{\varepsilon} \nabla \cdot \mathbf{v}_0' = \nabla^2 [(T_0 - T_{\mathrm{LNB}}) s_{0*}'], \qquad (3)$$

where ε is a friction parameter, f_0 is the Coriolis parameter, v_0' is the difference in surface wind between CNTL and SMTH, and the other quantities are the same as in section 5b.

The novelty of the diagnostic when compared to Lindzen and Nigam (1987), Minobe et al. (2008), and Takatama et al. (2012) is in the fact that the SLP difference between the two simulations, in the particular context of a cold air outbreak, is set by moist convection. The lower troposphere over the warm ocean is efficiently mixed in the vertical because of buoyant convection forced by surface turbulent heat fluxes. This mixing is limited in the vertical by an inversion located at a height of 2–3 km. The inversion resulting from a balance between large-scale subsidence and penetrative convection forced by surface buoyancy fluxes plays a similar role as the trade inversion in Lindzen and Nigam (1987). The time needed by surface fluxes to modify the temperature and humidity in the bulk of the boundary layer explains why convection occurs downstream of the SST front. Moreover, the first term in the Laplacian on the rhs of Eq. (3) differs from the first term on the rhs of Eq. (2) only by the lower limit chosen for the vertical integration (surface as opposed to level of free convection). The similarity of these two terms emphasizes the role of convection in controlling the pressure anomaly in the boundary layer that drives the anomalous circulation.

We calculated the surface wind divergence following the expression in Eq. (3). The prediction for surface wind convergence from Eq. (3) is illustrated in Fig. 6c with the following choice of parameters: Coriolis parameter $f = 10^{-4}\,\text{s}^{-1}$, drag coefficient $C_d = 1.8 \times 10^{-3}$, mean boundary layer wind in the cold sector $\|\mathbf{U}\| = 17\,\text{m\,s}^{-1}$, and averaged height of the boundary layer in the cold sector $H_{BL} = 2000\,\text{m}$ (conclusions are insensitive to the choice of the boundary layer height). According to this simple model, convergence of anomalous wind is expected on the warm side of the Gulf Stream, in close agreement with the anomalous circulation simulated in UM (Fig. 6b).

The slight discrepancies between the modeled and analytic surface wind convergence west of 70°W (cf. Figs. 6b and 6c) might arise from the physical processes we have neglected in our assumptions and in particular the vertical transport of momentum across the top of the boundary layer (Takatama et al. 2012).

6. Conclusions and discussion

The present study reconciles the explanation given for several climatological features of the Gulf Stream region and demonstrates the close connection between air–sea interactions during cold air outbreaks and the climatological band of precipitation. To evaluate the impact of air–sea interactions in the cold sector, we followed the strategy of Minobe et al. (2008) and forced a regional mesoscale model by two different sets of SSTs, either observed (CNTL) or with smoothed gradients (SMTH). The setup used here, with the same boundary conditions applied at the edge of the domain, is complementary to Minobe et al.'s (2008) experiments and makes it possible to isolate the effect of the SST gradient on the same extratropical cyclone. The main result of these experiments is that a band of precipitation following the line of the SST gradient was simulated during the course of a single storm as it was in their study for a 5-yr climatology. This first result is substantial as it suggests that some key mechanisms leading to an increase of precipitation on the warm edge of the SST front do not require a long stabilized simulation.

Several features simulated during the cold air outbreak are reminiscent of the findings of previous studies. First, the excess of precipitation in CNTL compared to SMTH is predominantly convective rain. This result is consistent with Kuwano-Yoshida et al. (2010), who showed that in a simulation of ½°, the impact of the SST gradient for a 5-yr mean was an anomalous band of convective precipitation. Second, the enhanced low-level convergence and the

associated meridional secondary circulation across the SST gradient simulated in this study are consistent with the observed surface wind convergence (Chelton et al. 2004; Minobe et al. 2008), and the enhanced ascent extends into the midtroposphere (Minobe et al. 2010). The secondary circulation associated with the occurrence of low-level cloud unraveled by Liu et al. (2014) is observed in this study.

The mechanism leading to an increase of convective precipitation and a cross-frontal circulation cell in CNTL is summarized in Fig. 13. After the passage of the cold front, the contrast of cold and dry air blowing from the continent over warmer waters generates intense turbulent heat fluxes. The boundary layer mixing scheme and convection scheme work together to homogenize the whole depth of the boundary layer. The same sequence of processes was observed in CNTL and SMTH. The effect of the different SSTs was to modulate the timing of this sequence and its spatial distribution. In CNTL and on the warm edge of the front, shallow convection develops earlier and the amount of convective rain increases. On the contrary, convection is reduced over the cold edge of the SST front. A simple MABL model showed that the history of the heat fluxes seen by the parcels flowing from the land in the two experiments could explain the difference in convective available potential energy and convective rain in the two experiments. We stress that the onset of the cumulus convection is related to the direct SST forcing and not to the SST gradient. In addition, the differential convection on both sides of the SST gradient in CNTL sets a dipole of anomalous boundary layer pressure that drives the anomalous circulation cell (cross section labeled B in Fig. 13). Vertical ascent is enhanced up to 500 hPa on the warm edge of the SST front in CNTL. The low-level humidity convergence associated with this secondary circulation is in balance with the anomalous convective precipitation in CNTL. Upstream of the cold-sector convective region (cross section labeled A in Fig. 13), the boundary layer pressure did not have time to adjust and to produce a cross-frontal circulation cell. In SMTH, the SST gradient and the differential convection are too weak to generate an anomalous circulation (cross section labeled C).

The mechanism suggested here gives a slightly different picture from the mechanism presented so far in the literature. The effect of the SST gradient is more to generate a north–south contrast of SST, modulating convection, than to have a direct dynamical effect on the circulation. We did not find a secondary circulation along the flow that would be directly induced by the SST gradient as in Huang and
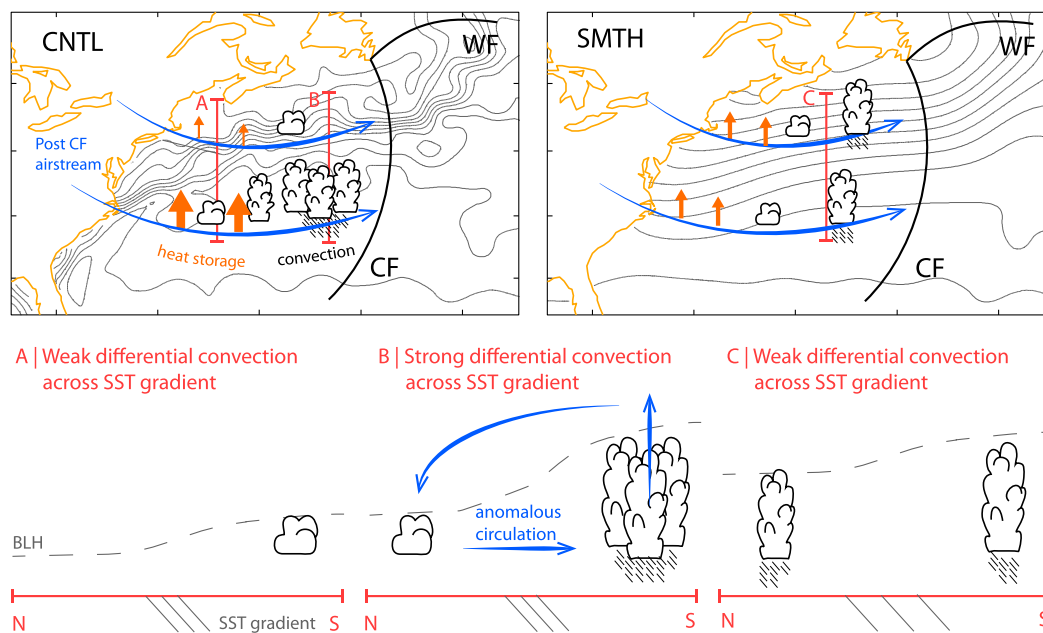
FIG. 13. (top) Schematic of the cold-sector air–sea interactions in (left) CNTL and (right) SMTH. Black lines denote the warm front (WF) and cold front (CF). SST contours in gray are shown with interval of 2 K. The blue arrows give the direction of the airflow. The size of orange arrows symbolizes the intensity of the surface heat fluxes. (bottom) North–south cross sections in the cold sector of CNTL (labeled A and B) and SMTH (labeled C) as depicted in (top).

Raman (1988), Wai and Stage (1989), and Liu et al. (2014). We did, however, observe a difference in wind convergence but far downwind of the North American coast and a secondary circulation but perpendicular to the background wind. As suggested by Small et al. (2008), the interaction of the boundary layer dynamics with the SST gradient depends on both the resolution of the model and the intensity of the background wind. Thus, further work needs to confirm the relevance of the proposed mechanism with various model resolutions. Yamamoto (2012) showed that there exists a large diversity of cold air outbreaks in the western North Pacific basin. If this is also the case in the western North Atlantic basin, and since Spall (2007) suggested that the background wind may lead to a different balance in the momentum equation, it could be interesting to test the significance of our results under different background conditions.

The novelty of the diagnostic boundary layer model proposed in this study when compared to Lindzen and Nigam (1987), Minobe et al. (2008), and Takatama et al. (2015), in the particular context of a cold air outbreak, is that it puts emphasis on the role of moist convection. Indeed, it shows that the lower troposphere over the warm ocean is efficiently mixed in the vertical because of moist convection forced by surface turbulent fluxes. This mixing

is limited in the vertical by an inversion located at a height of 2–3 km. The inversion results from a balance between large-scale subsidence and penetrative convection forced by surface fluxes in a similar way as the trade inversion in Lindzen and Nigam (1987). The enhanced convection over the warm side of the SST front causes negative SLP anomalies further driving the convection cell across the SST front. This is in line with Minobe et al. (2008), as their MABL model and ours are two equivalent points of view, when moist convection occurs in the cold sector.

The cold-sector air–sea interactions presented in this paper form a potential "cold path" by which the Gulf Stream front anchors atmospheric mean state features. Such a cold path would explain why the band of precipitation almost disappears during summer, as the weaker heat fluxes are less susceptible to destabilize the low-level atmosphere. It would also explain why the response of vertical wind to the SST gradient is restricted to the lower troposphere in winter [as shown by Minobe et al. (2010)], as this is consistent with the strongly stratified midtroposphere and subsidence of the cold sector. The long term effect of the cold path on the atmospheric climatology is currently investigated and will be the subject of another study.

APPENDIX

MABL Model for the Cold Sector

In the following, we recast the MABL model proposed by Minobe et al. (2008) to account for the pressure anomalies set by the convective adjustment in the bulk of boundary layer. Following Lindzen and Nigam (1987) and Minobe et al. (2008), the equations of motion in pressure coordinates read as follows:

$$-fv' = -\left(\frac{\partial \phi'}{\partial x}\right)_{p,y} + g\left(\frac{\partial F}{\partial p}\right)_{x,y}, \tag{A1}$$

$$fu' = -\left(\frac{\partial \phi'}{\partial y}\right)_{p,x} + g\left(\frac{\partial G}{\partial p}\right)_{x,y}, \quad \text{and} \tag{A2}$$

$$\left(\frac{\partial \phi'}{\partial p}\right)_{x,y} = \alpha', \tag{A3}$$

where u and v are, respectively, the zonal and meridional components of the horizontal wind, f is the Coriolis parameter, ϕ is the geopotential, F and G are the x and y components of the small-scale Reynolds stress, $\alpha = RT/p$, with R the gas constant, and the subscripts denote whether x, y, or pressure p is kept constant.

Differentiating Eqs. (A1) and (A2) once with respect to pressure and using Eq. (A3), we obtain the following:

$$-f\left(\frac{\partial v'}{\partial p}\right)_{x,y} = \left(\frac{\partial \alpha'}{\partial x}\right)_{p,y} + g\left(\frac{\partial^2 F}{\partial p^2}\right)_{x,y} \quad \text{and} \tag{A4}$$

$$f\left(\frac{\partial u'}{\partial p}\right)_{x,y} = \left(\frac{\partial \alpha'}{\partial y}\right)_{p,x} + g\left(\frac{\partial^2 G}{\partial p^2}\right)_{x,y}. \tag{A5}$$

Following Emanuel (1994) and using Maxwell's relations, we can relate the fluctuations of the parcel's specific volume $(\delta\alpha)_{par}$ at constant pressure to the fluctuations in the parcel's saturated moist entropy δs^*_{par}:

$$(\delta\alpha)_{par} = \left(\frac{\partial \alpha}{\partial s^*_{par}}\right)_p \delta s^*_{par} = \left(\frac{\partial T}{\partial p}\right)_{s_*} \delta s^*_{par}. \tag{A6}$$

Making use of Eq. (A6), it follows that

$$\left(\frac{\partial \alpha'}{\partial x}\right)_{p,y} = \left(\frac{\partial T}{\partial p}\right)_{y,s_*} \left(\frac{\partial s'_*}{\partial x}\right)_{p,y} \quad \text{and} \tag{A7}$$

$$\left(\frac{\partial \alpha'}{\partial y}\right)_{p,x} = \left(\frac{\partial T}{\partial p}\right)_{x,s_*} \left(\frac{\partial s'_*}{\partial y}\right)_{p,x}. \tag{A8}$$

Dropping the subscripts x, y, and p in the partial derivatives, we thus obtain the following:

$$-f\frac{\partial v'}{\partial p} = \left(\frac{\partial T}{\partial p}\right)_{s_*}\frac{\partial s'_*}{\partial x} + g\frac{\partial^2 F}{\partial p^2} \quad \text{and} \tag{A9}$$

$$f\frac{\partial u'}{\partial p} = \left(\frac{\partial T}{\partial p}\right)_{s_*}\frac{\partial s'_*}{\partial y} + g\frac{\partial^2 G}{\partial p^2}. \tag{A10}$$

Now, we introduce the key assumptions that both (u', v') and $(\partial F/\partial p, \partial G/\partial p)$ vanish just above the boundary layer (it can be seen on Fig. 8 that at an altitude of 2000 m, corresponding to the mean boundary layer top, horizontal wind anomalies are much weaker than at the surface). Using Eqs. (A1) and (A2), this implies that $\partial\phi'/\partial x = \partial\phi'/\partial y = 0$ just above the boundary layer. This is similar to the assumption made by Lindzen and Nigam (1987) in their boundary layer model without a "back pressure adjustment." In addition, we also assume that whenever convection is present in the cold sector, the saturation moist entropy does not vary significantly with height (this is a statement that convection is rapid enough to bring the lower atmosphere to a state of neutrality to vertical displacement of parcels from low levels; e.g., Emanuel 1994). Interestingly, the large-scale subsidence present in the cold sector in our model plays a similar role to the large-scale subsidence of the Hadley cell in Lindzen and Nigam's (1987) model.

Integrating vertically Eqs. (A9) and (A10) from the surface (denoted by the subscript 0) to above the boundary layer top (BL), we obtain the following, using the above assumptions:

$$-fv'_0 = \int_{p_{BL}}^{p_0} \left(\frac{\partial T}{\partial p}\right)_{s_*}\frac{\partial s'_*}{\partial x}dp - \varepsilon u'_0 \quad \text{and} \tag{A11}$$

$$fu'_0 = \int_{p_{BL}}^{p_0} \left(\frac{\partial T}{\partial p}\right)_{s_*}\frac{\partial s'_*}{\partial y}dp - \varepsilon v'_0. \tag{A12}$$

In the above, we have used the following model for the surface stress:

$$g\left(\frac{\partial F}{\partial p}\right)_{p=p_0} = -\varepsilon u'_0 \quad \text{and} \tag{A13}$$

$$g\left(\frac{\partial G}{\partial p}\right)_{p=p_0} = -\varepsilon v'_0. \tag{A14}$$

After a bit of algebra and assuming f varies according to the β-plane approximation, we obtain the following:

$$\frac{\varepsilon^2 + f_0^2}{\varepsilon}\nabla \cdot \mathbf{v}_0' = \nabla^2[(T_0 - T_{\text{LNB}})s_{0*}'] - \frac{\beta}{\varepsilon}(\varepsilon u_0' - f v_0'). \tag{A15}$$

The dimensionless number obtained from the ratio of the second term on the rhs to the first term on the lhs has the order of magnitude of $\beta L_y/f$ (with L_y the meridional scale of the surface wind divergence dipole) and quantifies the relative importance of those terms. Assuming L_y is 500 km, we obtain $\beta L_y/f \approx 0.1$, and the second term on the rhs can be neglected. The key Eq. (3) in section 5c follows immediately.

Finally, we want to draw the reader's attention to the relationship between our model and Minobe et al. (2008), who related the surface wind divergence to the Laplacian of SLP. In the following, we demonstrate that when moist convection occurs in the cold sector, those two points of view are equivalent. For the sake of simplicity the demonstration is made for the x component only. Equation (A7) can be written as follows:

$$\frac{\partial}{\partial p}\left(\frac{\partial \phi'}{\partial x}\right) = -\left(\frac{\partial T}{\partial p}\right)_{s_*}\frac{\partial s_*'}{\partial x}. \tag{A16}$$

If we neglect $\partial \phi'/\partial x$ at the boundary layer top, we get the following, after vertical integration from the sea surface to the top of the boundary layer:

$$\left(\frac{\partial \phi'}{\partial x}\right)_{p=p_0} = -(T_0 - T_{\text{BL}})\frac{\partial s_*'}{\partial x}. \tag{A17}$$

Using the approximation $\phi' \approx \text{SLP}'/\rho_o$, where ρ_o is an average density in the boundary layer, this can be rewritten as follows:

$$\frac{1}{\rho_0}\left(\frac{\partial \text{SLP}'}{\partial x}\right) = -(T_0 - T_{\text{BL}})\frac{\partial s_*'}{\partial x}. \tag{A18}$$

After taking another x derivative, applying the same method to get the second y derivative of SLP', and using Eq. (A15) with the β term neglected, this can be compared with Eq. (3) to find that divergence is proportional to the Laplacian of SLP in this model as in Minobe et al. (2008).

REFERENCES

Arakawa, A., and V. R. Lamb, 1977: Computational design of the basic dynamical processes of the UCLA general circulation model. *Methods Comput. Phys.*, **17**, 173–265.

Bond, N. A., M. F. Cronin, and M. Garvert, 2010: Atmospheric sensitivity to SST near the Kuroshio Extension during the extratropical transition of typhoon Tokage. *Mon. Wea. Rev.*, **138**, 2644–2663, doi:10.1175/2010MWR3198.1.

Brachet, S., F. Codron, Y. Feliks, M. Ghil, H. Le Treut, and E. Simonnet, 2012: Atmospheric circulations induced by a midlatitude SST front: A GCM study. *J. Climate*, **25**, 1847–1853, doi:10.1175/JCLI-D-11-00329.1.

Charney, J. G., and N. Phillips, 1953: Numerical integration of the quasi-geostrophic equations for barotropic and simple baroclinic flows. *J. Meteor.*, **10**, 71–99, doi:10.1175/1520-0469(1953)010<0071:NIOTQG>2.0.CO;2.

Chelton, D. B., M. G. Schlax, M. H. Freilich, and R. F. Milliff, 2004: Satellite measurements reveal persistent small-scale features in ocean winds. *Science*, **303**, 978–983, doi:10.1126/science.1091901.

Cronin, M. F., S.-P. Xie, and H. Hashizume, 2003: Barometric pressure variations associated with eastern Pacific tropical instability waves. *J. Climate*, **16**, 3050–3057, doi:10.1175/1520-0442(2003)016<3050:BPVAWE>2.0.CO;2.

Davies, T., M. Cullen, A. Malcolm, M. Mawson, A. Staniforth, A. White, and N. Wood, 2005: A new dynamical core for the Met Office's global and regional modelling of the atmosphere. *Quart. J. Roy. Meteor. Soc.*, **131**, 1759–1782, doi:10.1256/qj.04.101.

de Szoeke, S. P., and C. Bretherton, 2004: Quasi-Lagrangian large eddy simulations of cross-equatorial flow in the east Pacific atmospheric boundary layer. *J. Atmos. Sci.*, **61**, 1837–1858, doi:10.1175/1520-0469(2004)061<1837:QLESOC>2.0.CO;2.

ECMWF, 2011: ECMWF's Operational Model Analysis, starting in 2011. Research Data Archive at the National Center for Atmospheric Research, Computational and Information Systems Laboratory, accessed 22 October 2013, doi:10.5065/D6ZG6Q9F.

Edwards, J., and A. Slingo, 1996: Studies with a flexible new radiation code. I: Choosing a configuration for a large-scale model. *Quart. J. Roy. Meteor. Soc.*, **122**, 689–719, doi:10.1002/qj.49712253107.

Emanuel, K. A., 1994: *Atmospheric Convection*. Oxford University Press, 592 pp.

Field, P. R., and R. Wood, 2007: Precipitation and cloud structure in midlatitude cyclones. *J. Climate*, **20**, 233–254, doi:10.1175/JCLI3998.1.

Giordani, H., and G. Caniaux, 2001: Sensitivity of cyclogenesis to sea surface temperature in the northwestern Atlantic. *Mon. Wea. Rev.*, **129**, 1273–1295, doi:10.1175/1520-0493(2001)129<1273:SOCTSS>2.0.CO;2.

Gregory, D., and P. Rowntree, 1990: A mass flux convection scheme with representation of cloud ensemble characteristics and stability-dependent closure. *Mon. Wea. Rev.*, **118**, 1483–1506, doi:10.1175/1520-0493(1990)118<1483:AMFCSW>2.0.CO;2.

——, and S. Allen, 1991: The effect of convective scale downdrafts upon NWP and climate simulations. Preprints, *Ninth Conf. on Numerical Weather Prediction*, Denver, CO, Amer. Meteor. Soc., 122–123.

——, R. Kershaw, and P. Inness, 1997: Parametrization of momentum transport by convection. II: Tests in single-column and general circulation models. *Quart. J. Roy. Meteor. Soc.*, **123**, 1153–1183, doi:10.1002/qj.49712354103.

Hashizume, H., S.-P. Xie, M. Fujiwara, M. Shiotani, T. Watanabe, Y. Tanimoto, W. T. Liu, and K. Takeuchi, 2002: Direct observations of atmospheric boundary layer response to SST variations associated with tropical instability waves over the eastern equatorial Pacific. *J. Climate*, **15**, 3379–3393, doi:10.1175/1520-0442(2002)015<3379:DOOABL>2.0.CO;2.

Huang, C.-Y., and S. Raman, 1988: A numerical modeling study of the marine boundary layer over the Gulf Stream during cold

air advection. *Bound.-Layer Meteor.*, **45**, 251–290, doi:10.1007/BF01066673.

Huffman, G. J., and Coauthors, 2007: The TRMM Multisatellite Precipitation Analysis (TMPA): Quasi-global, multiyear, combined-sensor precipitation estimates at fine scales. *J. Hydrometeor.*, **8**, 38–55, doi:10.1175/JHM560.1.

Konda, M., H. Ichikawa, H. Tomita, and M. F. Cronin, 2010: Surface heat flux variations across the Kuroshio Extension as observed by surface flux buoys. *J. Climate*, **23**, 5206–5221, doi:10.1175/2010JCLI3391.1.

Kuwano-Yoshida, A., S. Minobe, and S.-P. Xie, 2010: Precipitation response to the Gulf Stream in an atmospheric GCM. *J. Climate*, **23**, 3676–3698, doi:10.1175/2010JCLI3261.1.

Lanczos, C., 1988: *Applied Analysis*. Prentice Hall, 539 pp.

Lindzen, R. S., and S. Nigam, 1987: On the role of sea surface temperature gradients in forcing low-level winds and convergence in the tropics. *J. Atmos. Sci.*, **44**, 2418–2436, doi:10.1175/1520-0469(1987)044<2418:OTROSS>2.0.CO;2.

Liu, J.-W., S.-P. Xie, J. R. Norris, and S.-P. Zhang, 2014: Low-level cloud response to the Gulf Stream front in winter using *CALIPSO*. *J. Climate*, **27**, 4421–4432, doi:10.1175/JCLI-D-14-00469.1.

Lock, A., A. Brown, M. Bush, G. Martin, and R. Smith, 2000: A new boundary layer mixing scheme. Part I: Scheme description and single-column model tests. *Mon. Wea. Rev.*, **128**, 3187–3199, doi:10.1175/1520-0493(2000)128<3187:ANBLMS>2.0.CO;2.

Minobe, S., A. Kuwano-Yoshida, N. Komori, S.-P. Xie, and R. J. Small, 2008: Influence of the Gulf Stream on the troposphere. *Nature*, **452**, 206–209, doi:10.1038/nature06690.

——, M. Miyashita, A. Kuwano-Yoshida, H. Tokinaga, and S.-P. Xie, 2010: Atmospheric response to the Gulf Stream: Seasonal variations. *J. Climate*, **23**, 3699–3719, doi:10.1175/2010JCLI3359.1.

Nelson, J., and R. He, 2012: Effect of the Gulf Stream on winter extratropical cyclone outbreaks. *Atmos. Sci. Lett.*, **13**, 311–316, doi:10.1002/asl.400.

Parfitt, R., and A. Czaja, 2016: On the contribution of synoptic transients to the mean atmospheric state in the Gulf Stream region. *Quart. J. Roy. Meteor. Soc.*, **142**, 1554–1561, doi:10.1002/qj.2689.

Plagge, A., J. B. Edson, and D. Vandemark, 2016: In situ and satellite evaluation of air–sea flux variation near ocean temperature gradients. *J. Climate*, **29**, 1583–1602, doi:10.1175/JCLI-D-15-0489.1.

Sanders, F., and J. R. Gyakum, 1980: Synoptic-dynamic climatology of the bomb. *Mon. Wea. Rev.*, **108**, 1589–1606, doi:10.1175/1520-0493(1980)108<1589:SDCOT>2.0.CO;2.

Skyllingstad, E. D., and J. B. Edson, 2009: Large-eddy simulation of moist convection during a cold air outbreak over the Gulf Stream. *J. Atmos. Sci.*, **66**, 1274–1293, doi:10.1175/2008JAS2755.1.

——, D. Vickers, L. Mahrt, and R. Samelson, 2007: Effects of mesoscale sea-surface temperature fronts on the marine atmospheric boundary layer. *Bound.-Layer Meteor.*, **123**, 219–237, doi:10.1007/s10546-006-9127-8.

Small, R. J., S.-P. Xie, and Y. Wang, 2003: Numerical simulation of atmospheric response to Pacific tropical instability waves. *J. Climate*, **16**, 3723–3741, doi:10.1175/1520-0442(2003)016<3723:NSOART>2.0.CO;2.

——, ——, ——, S. K. Esbensen, and D. Vickers, 2005: Numerical simulation of boundary layer structure and cross-equatorial flow in the eastern Pacific. *J. Atmos. Sci.*, **62**, 1812–1830, doi:10.1175/JAS3433.1.

——, ——, L. O. Ńeill, H. Seo, Q. Song, P. Cornillon, M. Spall, and S. Minobe, 2008: Air–sea interaction over ocean fronts and eddies. *Dyn. Atmos. Oceans*, **45**, 274–319, doi:10.1016/j.dynatmoce.2008.01.001.

Song, Q., P. Cornillon, and T. Hara, 2006: Surface wind response to oceanic fronts. *J. Geophys. Res.*, **111**, C12006, doi:10.1029/2006JC003680.

Spall, M. A., 2007: Effect of sea surface temperature–wind stress coupling on baroclinic instability in the ocean. *J. Phys. Oceanogr.*, **37**, 1092–1097, doi:10.1175/JPO3045.1.

Stratton, R., A. Stirling, and S. Derbyshire, 2009: Changes and developments to convective momentum transport (CMT) parametrization based on analysis of CRM and SCM. Met Office R&D Tech. Rep. 530.

Sublette, S., and G. S. Young, 1996: Warm-season effects of the Gulf Stream on mesoscale characteristics of the atmospheric boundary layer. *Mon. Wea. Rev.*, **124**, 653–667, doi:10.1175/1520-0493(1996)124<0653:WSEOTG>2.0.CO;2.

Sweet, W., R. Fett, J. Kerling, and P. La Violette, 1981: Air-sea interaction effects in the lower troposphere across the north wall of the Gulf Stream. *Mon. Wea. Rev.*, **109**, 1042–1052, doi:10.1175/1520-0493(1981)109<1042:ASIEIT>2.0.CO;2.

Takatama, K., S. Minobe, M. Inatsu, and R. J. Small, 2012: Diagnostics for near-surface wind convergence/divergence response to the Gulf Stream in a regional atmospheric model. *Atmos. Sci. Lett.*, **13**, 16–21, doi:10.1002/asl.355.

——, ——, ——, and ——, 2015: Diagnostics for near-surface wind response to the Gulf Stream in a regional atmospheric model. *J. Climate*, **28**, 238–255, doi:10.1175/JCLI-D-13-00668.1.

Tokinaga, H., Y. Tanimoto, and S.-P. Xie, 2005: SST-induced surface wind variations over the Brazil–Malvinas confluence: Satellite and in situ observations. *J. Climate*, **18**, 3470–3482, doi:10.1175/JCLI3485.1.

Vannière, B., A. Czaja, H. Dacre, T. Woollings, and R. Parfitt, 2015: A potential vorticity signature for the cold sector of extratropical cyclones. *Quart. J. Roy. Meteor. Soc.*, **142**, 432–442, doi:10.1002/qj.2662.

Wai, M. M.-K., and S. A. Stage, 1989: Dynamical analyses of marine atmospheric boundary layer structure near the Gulf Stream oceanic front. *Quart. J. Roy. Meteor. Soc.*, **115**, 29–44, doi:10.1002/qj.49711548503.

Wallace, J. M., T. Mitchell, and C. Deser, 1989: The influence of sea-surface temperature on surface wind in the eastern equatorial Pacific: Seasonal and interannual variability. *J. Climate*, **2**, 1492–1499, doi:10.1175/1520-0442(1989)002<1492:TIOSST>2.0.CO;2.

Wayland, R. J., and S. Raman, 1989: Mean and turbulent structure of a baroclinic marine boundary layer during the 28 January 1986 cold-air outbreak (GALE 86). *Bound.-Layer Meteor.*, **48**, 227–254, doi:10.1007/BF00158326.

Wilson, D. R., and S. P. Ballard, 1999: A microphysically based precipitation scheme for the UK Meteorological Office unified model. *Quart. J. Roy. Meteor. Soc.*, **125**, 1607–1636, doi:10.1002/qj.49712555707.

Xie, S.-P., 2004: Satellite observations of cool ocean–atmosphere interaction. *Bull. Amer. Meteor. Soc.*, **85**, 195–208, doi:10.1175/BAMS-85-2-195.

Yamamoto, M., 2012: Mesoscale structures of two types of cold-air outbreaks over the East China Sea and the effect of coastal sea surface temperature. *Meteor. Atmos. Phys.*, **115**, 89–112, doi:10.1007/s00703-011-0176-2.

Young, G. S., and T. D. Sikora, 2003: Mesoscale stratocumulus bands caused by Gulf Stream meanders. *Mon. Wea. Rev.*, **131**, 2177–2191, doi:10.1175/1520-0493(2003)131<2177:MSBCBG>2.0.CO;2.

Zolina, O., and S. K. Gulev, 2003: Synoptic variability of ocean–atmosphere turbulent fluxes associated with atmospheric cyclones. *J. Climate*, **16**, 2717–2734, doi:10.1175/1520-0442(2003)016<2717:SVOOTF>2.0.CO;2.